

The abundance pattern of O, Mg, Si and Fe in the intracluster medium of the Centaurus cluster observed with XMM-Newton

Kyoko Matsushita^{1,2}, Hans Böhringer², Isao Takahashi³, Yasushi Ikebe⁴

¹ Department of Physics, Tokyo University of Science, 1-3 Kagurazaka, Shinjuku-ku, Tokyo, 162-8601 Japan

² Max-Planck-Institut für Extraterrestrial Physik, D-85748 Garching, Germany

³ Department of Physics, University of Tokyo, 7-3-1 Hongo, Bunkyo-ku, Tokyo, 113-8654 Japan,

⁴ Joint Center for Astrophysics, University of Maryland, Baltimore County, 1000 Hilltop Circle, Baltimore, MD 21250, USA

Abstract. The abundances of O, Mg, Si and Fe in the intracluster medium of the Centaurus cluster are derived. The Fe abundance has a negative radial gradient. In solar units, the Si abundance is close to the Fe abundance, while the O and Mg abundances are much smaller. The high Fe/O and Si/O ratio indicate that metal supply from supernovae Ia is important and supernovae Ia synthesize Si as well as Fe. Within 2', the O and Mg abundances are consistent with the stellar metallicity of the cD galaxy derived from the Mg₂ index. This result indicates that the central gas is dominated by the gas from the cD galaxy. The observed abundance pattern of the Centaurus cluster resembles to those observed in center of other clusters and groups of galaxies. However, the central Fe abundance and the Si/Fe ratio are 40 % higher and 30% smaller than those of M 87, respectively. Since the accumulation timescale of the supernovae Ia is higher in the Centaurus cluster, these differences imply a time dependence of nucleosynthesis by supernovae Ia.

Key words. X-rays:ICM — galaxies:ISM — individual:Centaurus cluster

1. Introduction

The intracluster medium (ICM) contains a large amount of metals, which are synthesized by supernovae (SNe) Ia and SNe II in cluster galaxies. A knowledge of the contributions from the two types of SNe to the metal abundances are important to understand the origin of the metals and to study the evolution of galaxies in clusters.

The XMM-Newton observatory enables us to derive O and Mg abundances, which are not synthesized by SN Ia. For the ICM of M 87 observed with the XMM, the O/Si ratio is found to be about a half of the solar ratio, while Fe and Si have similar values in units of the solar abundance (Böhringer et al. 2001; Finoguenov et al. 2002; Matsushita et al. 2003). Such low O abundances compared to the Si abundances are also derived for the centers of other clusters and groups of galaxies (e.g. Tamura et al. 2001b ; Boute et al. 2003, and others).

In order to account for the observed O/Si/Fe abundance pattern of M 87, the Fe/Si ratio of ejecta of SN Ia should be about 1 solar ratio. This value is significantly higher than expected and probably related with dimmer SNe Ia observed in old stellar systems (Hamuy et al. 1996; Ivanov et al. 2000). Since the mass of synthesized Ni⁵⁶ de-

termines the luminosity of each SN, the abundance ratio in the ejecta may be correlated to the luminosity of SN Ia. In this context a lower Ni⁵⁶ yield implies less complete nuclear burning with a higher ratio of α -elements such as Si to Fe. The observed O/Si/Fe pattern of the Galactic stars also indicates that the Si/Fe ratio in ejecta of SN Ia depends on stellar metallicity, i.e., age of the system (Matsushita et al. 2003)

The variation in the observed abundance pattern reflects variations in the explosion models, e.g. a high fraction of Fe for the classical deflagration model, W7 (Nomoto et al. 1984) or a larger fraction of Si for the delayed detonation model, WDDs (Nomoto et al. 1997; Iwamoto et al. 1999). The W7 model, which can well reproduce observed optical spectra of SNe Ia (Nugent et al. 1997), predicts a high Fe/Si ratio of 2.6 in units of the solar ratio. In contrast, the WDD models give a wider range of Fe/Si ratios from 1 to 3 in units of the solar ratio, which might be related to the age of the system (Umeda et al. 1999).

In this paper, we report on the O/Mg/Si/Fe abundance pattern of the Centaurus cluster observed with XMM. The temperature properties of the cluster are described in Takahashi (2004). The Centaurus cluster is a nearby cluster, centered on the cD galaxy, NGC 4696. A positive temperature gradient and a negative abun-

dance gradient are observed with ASCA (Fukazawa et al. 1994; Ikebe et al. 1999). The cluster is expected to have a cooling flow (Allen & Fabian 1994), and Chandra observed an unusual plume-like cool structure at the center (Sanders & Fabian 2002). However, as in other cooling flow clusters, the luminosity of the central cool component is much smaller than the expected value from the cooling flow model (e.g. Makishima et al. 2001; Tamura et al. 2001a; Böhringer et al. 2002; Matsushita et al. 2002). The problem of the missing of the cooling component becomes an advantage in determination of elemental abundances, since the observed narrow temperature range of the ICM strongly reduces the ambiguity in the abundance measurement.

We adopt for the solar abundances the values given by Feldman (1992), where the solar Fe abundance relative to H is 3.24×10^{-5} in number. A value for the Hubble constant of $H_0 = 70 \text{ km/s/Mpc}$ is assumed. Unless otherwise specified, we use 90% confidence error regions.

2. Observation

The Centaurus cluster was observed with XMM-Newton on January 3rd, 2002. The thin filter is used for the EMOS and the EPN. We have selected events with pattern smaller than 5 and 13 for the EPN and the EMOS, respectively. The background spectrum was calculated for each spectrum by integrating blank sky data in the same detector regions. Among deep sky observations collected with XMM, we have selected the data with the most similar background to that of the Centaurus cluster, after screening background flare events in the data and the background following Katayama et al. (2004). The effective exposures of the EPN and the EMOS are 29 ks and 32 ks, respectively. The spectra are accumulated within rings, centered on the X-ray peak of the cluster. After subtracting the background and correcting for the effect of vignetting, deprojected spectra are calculated assuming spherical symmetry. For the EPN spectra, the response matrix file and the auxiliary response file corresponding to each spectrum are calculated using SAS-v5.4.1. For the EMOS data, we used m1_thin1v9q20t5r6_all_15.rsp. The spectral analysis uses the XSPEC_v11.2.0 package. For the EPN data, we used the spectral range from 0.5 to 7.3 keV, in order to discard strong instrumental lines around 8 keV. We fitted the EMOS data in the spectral range from 0.4 to 9.0 keV. At $r > 8'$, the energy range of 1.45–1.55 keV of the EMOS is discarded due to a strong instrumental line. Here, r is the projected radius from the X-ray peak. We also denote R as the deprojected or three-dimensional radius.

3. Spectral fit with the MEKAL model

The first step of the analysis is fitting the annular (projected) spectra with a single temperature MEKAL (e.g. Kaastra 1992; Liedahl et al. 1995) model, and the deprojected spectra with a single and two-temperature MEKAL

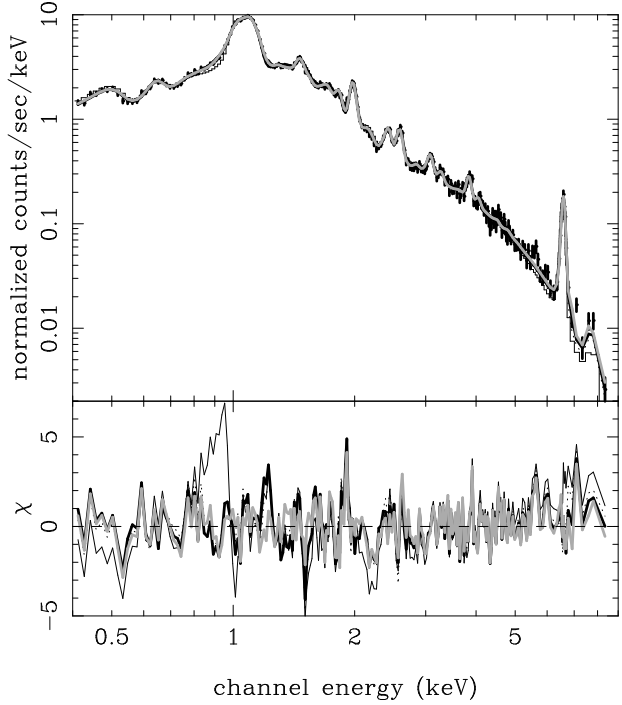


Fig. 1. The deprojected spectrum at $R=0.5\text{--}2'$ of the EMOS1+EMOS2 of the Centaurus cluster fitted with the single temperature MEKAL model (black thin lines), the two-temperature MEKAL model (black dotted lines), the multi-temperature MEKAL model (black bold lines), and the multi-temperature APEC model (gray bold lines).

model with photoelectric absorption. Abundances of C and N are fixed to be 1 solar and those of other elements are determined separately. The abundances of each element for all temperature components are assumed to have the same values. In addition, the deprojected spectra are fitted with a multi-temperature model which is a sum of 14 temperature components. Since a spectrum from an isothermal plasma can be well reproduced by a sum of spectra of plasma of two neighboring temperatures with similar elemental abundances, we selected temperatures in order to derive metal abundances with an accuracy within 5 %. Thus, in order to determine the abundance distribution, this multi-temperature model is enough to fit any temperature distribution at least when all temperature components have the same abundances.

Table 1 and 2 summarize the results. Even for the deprojected spectra, the single temperature model is not acceptable at $R < 2'$. The two-temperature model dramatically reduces the χ^2 , and the multi-temperature model slightly improves χ^2 . Outside this radius, χ^2 derived from the two- and the multi-temperature model are slightly smaller than those of the single-temperature model. Figure 1 shows a representative spectrum for $R=0.5\text{--}2'$. Using the two- and the multi-temperature MEKAL model, not only the continuum and the Fe-L bump, but also the strength of the Fe-K line is fitted well. The consistency between the Fe-L and the Fe-K will

Table 1. Results of spectrum fitting of the projected spectra.

<i>r</i> (arcmin)		kT (keV)		<i>N</i> _H (10 ²⁰ cm ⁻²)	O (solar)	Mg (solar)	Si (solar)	Fe (solar)	χ^2/dof	
0.05- 0.25	EMOS	1T	1.00	17.8	0.00	0.09	0.28	0.34	837/ 61	
0.25- 0.50	EMOS	1T	1.36	15.0	0.25	0.00	0.47	0.67	740/ 96	
0.50- 0.70	EMOS	1T	1.66	11.8	0.33	0.09	1.01	1.20	386/ 93	
0.70- 1.00	EMOS	1T	1.89	10.9	0.44	0.18	1.31	1.50	483/127	
1.00- 1.40	EMOS	1T	2.42 ^{+0.05} _{-0.05}	9.4 ^{+0.6} _{-0.6}	0.64 ^{+0.19} _{-0.18}	0.28	1.60 ^{+0.17} _{-0.16}	2.04 ^{+0.13} _{-0.12}	283/148	
1.40- 2.00	EMOS	1T	2.77 ^{+0.05} _{-0.05}	8.8 ^{+0.5} _{-0.5}	0.50 ^{+0.17} _{-0.16}	0.41	1.58 ^{+0.15} _{-0.14}	1.83 ^{+0.09} _{-0.09}	266/169	
2.00- 2.80	EMOS	1T	3.00 ^{+0.05} _{-0.05}	8.8 ^{+0.4} _{-0.5}	0.70 ^{+0.17} _{-0.16}	0.56	1.43 ^{+0.14} _{-0.13}	1.66 ^{+0.08} _{-0.08}	307/193	
2.80- 4.00	EMOS	1T	3.32 ^{+0.06} _{-0.06}	9.2 ^{+0.4} _{-0.4}	0.60 ^{+0.15} _{-0.15}	0.31	0.98 ^{+0.12} _{-0.12}	1.14 ^{+0.06} _{-0.06}	331/224	
4.00- 5.60	EMOS	1T	3.60 ^{+0.07} _{-0.07}	8.2 ^{+0.4} _{-0.3}	0.37 ^{+0.14} _{-0.14}	0.48	0.78 ^{+0.11} _{-0.11}	0.80 ^{+0.05} _{-0.05}	329/240	
5.60- 8.00	EMOS	1T	3.71 ^{+0.10} _{-0.08}	8.0 ^{+0.4} _{-0.4}	0.49 ^{+0.15} _{-0.15}	0.48	0.70 ^{+0.11} _{-0.11}	0.68 ^{+0.05} _{-0.05}	366/271	
8.00-13.50	EMOS	1T	3.75 ^{+0.12} _{-0.10}	7.3 ^{+0.4} _{-0.4}	0.43 ^{+0.14} _{-0.13}	0.84	0.62 ^{+0.11} _{-0.10}	0.57 ^{+0.05} _{-0.05}	439/325	
8.00-13.50	EMOS	2T	4.30 ^{+1.68} _{-0.29}	1.43 ^{+0.76} _{-0.21}	7.3 ^{+0.3} _{-0.4}	0.44 ^{+0.07} _{-0.13}	0.73	0.65 ^{+0.12} _{-0.13}	0.53 ^{+0.08} _{-0.11}	409/322
8.00-13.50	EMOS	14T			9.3 ^{+1.2} _{-1.3}	0.33 ^{+0.16} _{-0.08}	0.78	0.66 ^{+0.09} _{-0.09}	0.57 ^{+0.04} _{-0.06}	396/311
0.05- 0.25	EPN	1T	0.78	28.8	0.01	0.00	0.09	0.14	1151/139	
0.25- 0.50	EPN	1T	1.37	12.5	0.00	0.00	0.45	0.71	1087/201	
0.50- 1.00	EPN	1T	1.89	8.7	0.04	0.00	0.98	1.48	1044/343	
1.00- 1.40	EPN	1T	2.38 ^{+0.04} _{-0.04}	7.2 ^{+0.6} _{-0.7}	0.19 ^{+0.15} _{-0.13}	0.00	1.38 ^{+0.17} _{-0.13}	1.88 ^{+0.11} _{-0.08}	476/313	
1.40- 2.00	EPN	1T	2.70 ^{+0.04} _{-0.04}	7.2 ^{+0.5} _{-0.5}	0.25 ^{+0.13} _{-0.13}	0.08	1.29 ^{+0.14} _{-0.13}	1.68 ^{+0.08} _{-0.07}	459/364	
2.00- 2.80	EPN	1T	2.92 ^{+0.05} _{-0.04}	7.5 ^{+0.5} _{-0.6}	0.39 ^{+0.15} _{-0.13}	0.09	1.00 ^{+0.12} _{-0.11}	1.49 ^{+0.08} _{-0.06}	579/412	
2.80- 4.00	EPN	1T	3.25 ^{+0.05} _{-0.05}	7.3 ^{+0.5} _{-0.4}	0.06 ^{+0.11} _{-0.06}	0.20	0.82 ^{+0.11} _{-0.11}	1.06 ^{+0.05} _{-0.05}	533/472	
4.00- 5.60	EPN	1T	3.60 ^{+0.06} _{-0.04}	6.6 ^{+0.4} _{-0.4}	0.12 ^{+0.12} _{-0.12}	0.01	0.54 ^{+0.12} _{-0.12}	0.80 ^{+0.04} _{-0.04}	591/496	
5.60- 8.00	EPN	1T	3.84 ^{+0.07} _{-0.07}	6.1 ^{+0.4} _{-0.4}	0.05 ^{+0.12} _{-0.05}	0.05	0.40 ^{+0.11} _{-0.11}	0.65 ^{+0.04} _{-0.04}	579/527	
8.00-16.00	EPN	1T	3.98 ^{+0.14} _{-0.05}	5.7 ^{+0.3} _{-0.5}	0.04 ^{+0.16} _{-0.04}	0.00	0.36 ^{+0.11} _{-0.09}	0.63 ^{+0.06} _{-0.03}	805/687	
8.00-16.00	EPN	2T	4.14 ^{+0.17} _{-0.06}	1.06 ^{+0.08} _{-0.17}	6.2 ^{+0.4} _{-0.5}	0.24 ^{+0.14} _{-0.12}	0.01	0.44 ^{+0.11} _{-0.11}	0.66 ^{+0.05} _{-0.03}	746/684
8.00-16.00	EPN	14T			6.4 ^{+3.0} _{-0.4}	0.25 ^{+0.18} _{-0.13}	0.00	0.45 ^{+0.09} _{-0.10}	0.66 ^{+0.04} _{-0.05}	736/674

be discussed in detail at §4.3.3. There remains a residual structure around 1.2–1.5 keV at the Fe-L/Mg-K region. Therefore, in Table 1 and 2, we do not show errors in the Mg abundances.

The temperature of the ICM decreases sharply toward the center (Figure 2), and we need more than two temperature components to fit the deprojected spectra at the central region. The observed sharp temperature gradient means that the single temperature model is not enough to fit each deprojected spectrum, even if the ICM is isothermal locally. In addition, the cluster is not circularly symmetric and the cool plume-like structure at the center (Sanders & Fabian 2002) might introduce an additional temperature component.

The hydrogen column density, N_H is consistent with the Galactic value at $R > 1'$, although the EPN and the EMOS give slightly different results by a few times 10²⁰cm⁻² (Figure 2). Within $R < 1'$, the two- and the multi-temperature models give similar values to those of $R > 1'$. Higher column densities derived from the single temperature model fit within $R < 1'$ are not acceptable due to their high χ^2 . Therefore, N_H is consistent with the Galactic value within the whole field of view.

Discarding the results of unacceptable fits (reduced $\chi^2 > 2$), the Fe abundance is ~ 0.6 solar at $R > 8'$ and within the radius, it increases steeply toward center. Within 2', the gradient becomes weaker. The average value of the Fe abundance at $R < 2'$ is 2.3 solar (Figure 3). The EPN and the EMOS give consistent Fe abundances

within 10% (Table 2). The Fe abundances from the deprojected spectra are slightly higher than those from the projected spectra.

At each radius, the Si abundance is close to the Fe abundance (Figure 3, 4). The uncertainties in the Si/Fe ratio are better constrained than those in the Si and Fe abundances themselves (4), since the derived abundance of Si and Fe are correlated to each other. On average, the Si/Fe ratio is 0.89 \pm 0.04 and 0.75 \pm 0.04 in units of the solar ratio using the EMOS and EPN, respectively.

The O abundances are much smaller than the Si and Fe abundances (Figure 3, 4). The two detectors give inconsistent O abundances. Using the EMOS, the O abundance is about 0.8 solar at $R=0.5$ –2.0' and at $R > 2'$, it reduces to 0.4 solar (Figure 3), and the O/Fe ratio increases toward outer regions (Figure 4). In contrast, the EPN gives a significantly smaller O abundance than the EMOS especially in the outer regions (Figure 3), and the profile of the O/Fe ratio is consistent with no radial gradient (Figure 4).

In summary, as in center of other clusters and groups of galaxies, the Fe and Si abundances are close to each other with strong negative radial gradients. The O abundance is at least a factor of 2 smaller. The discrepancies in the O and Si abundances between the EMOS and EPN will be discussed in section 4.3.

Table 2. Results of spectrum fitting of the deprojected spectra

<i>R</i> (arcmin)		kT1 (keV)	kT2 (keV)	<i>N</i> _H (10 ²⁰ cm ⁻²)	O (solar)	Mg (solar)	Si (solar)	Fe (solar)	χ^2/dof	
0.00- 0.50	EMOS	1T	1.08	15.9	0.17	0.11	0.35	0.45	1111/129	
0.00- 0.50	EMOS	2T	1.51 ^{+0.05} _{-0.07}	0.71 ^{+0.01} _{-0.02}	11.4 ^{+2.4} _{-1.1}	0.49 ^{+0.18} _{-0.18}	0.89	1.30 ^{+0.23} _{-0.30}	1.57 ^{+0.24} _{-0.28} 169/126	
0.00- 0.50	EMOS	14T			11.4 ^{+3.7} _{-2.1}	0.48 ^{+0.25} _{-0.19}	0.89	1.39 ^{+0.46} _{-0.33}	1.79 ^{+0.42} _{-0.34} 139/116	
0.00- 0.50	EPN	1T	0.97		16.9	0.14	0.04	0.28	0.38	1167/176
0.00- 0.50	EPN	2T	1.45 ^{+0.07} _{-0.08}	0.70 ^{+0.02} _{-0.02}	11.6 ^{+1.2} _{-2.4}	0.59 ^{+0.29} _{-0.19}	0.80	1.52 ^{+0.45} _{-0.38}	1.85 ^{+0.29} _{-0.35} 195/173	
0.00- 0.50	EPN	14T			20.8 ^{+12.9} _{-7.5}	0.71 ^{+0.37} _{-0.28}	1.39	2.48 ^{+0.74} _{-1.00}	3.44 ^{+0.74} _{-1.26} 170/163	
0.50- 1.00	EMOS	1T	1.43		13.5	0.49	0.24	1.20	1.17	354/146
0.50- 1.00	EMOS	2T	1.74 ^{+0.07} _{-0.03}	0.85 ^{+0.03} _{-0.04}	9.7 ^{+1.3} _{-1.6}	1.15 ^{+0.45} _{-0.30}	1.26	2.79 ^{+0.72} _{-0.42}	2.71 ^{+0.57} _{-0.33} 189/143	
0.50- 1.00	EMOS	14T			9.3 ^{+1.2} _{-1.6}	1.22 ^{+0.47} _{-0.33}	1.43	3.06 ^{+0.72} _{-0.62}	2.93 ^{+0.56} _{-0.75} 189/133	
1.00- 2.00	EMOS	1T	2.30 ^{+0.06} _{-0.05}		8.8 ^{+0.8} _{-0.8}	0.49 ^{+0.22} _{-0.20}	0.34	1.83 ^{+0.22} _{-0.20}	2.22 ^{+0.18} _{-0.16} 246/212	
1.00- 2.00	EMOS	2T	2.46 ^{+0.25} _{-0.12}	1.30 ^{+0.31} _{-0.37}	8.7 ^{+0.8} _{-0.8}	0.62 ^{+0.24} _{-0.22}	0.53	2.07 ^{+0.27} _{-0.25}	2.42 ^{+0.23} _{-0.20} 220/209	
1.00- 2.00	EMOS	14T			8.6 ^{+1.0} _{-0.8}	0.62 ^{+0.25} _{-0.21}	0.58	2.12 ^{+0.28} _{-0.26}	2.44 ^{+0.22} _{-0.21} 214/199	
0.50- 2.00	EMOS	1T	1.95		10.2	0.40	0.20	1.42	1.70	658/249
0.50- 2.00	EMOS	2T	2.20 ^{+0.07} _{-0.05}	1.00 ^{+0.12} _{-0.08}	9.0 ^{+0.6} _{-0.6}	0.78 ^{+0.16} _{-0.16}	0.79	2.23 ^{+0.20} _{-0.20}	2.46 ^{+0.16} _{-0.16} 339/246	
0.50- 2.00	EMOS	14T			8.9 ^{+0.6} _{-0.7}	0.78 ^{+0.17} _{-0.15}	0.80	2.33 ^{+0.21} _{-0.21}	2.54 ^{+0.16} _{-0.17} 322/236	
0.50- 2.00	EPN	1T	2.10		7.6	0.08	0.00	1.24	1.73	1074/458
0.50- 2.00	EPN	2T	2.21 ^{+0.03} _{-0.03}	0.92 ^{+0.05} _{-0.07}	7.9 ^{+0.5} _{-0.6}	0.45 ^{+0.13} _{-0.09}	0.19	1.70 ^{+0.16} _{-0.10}	2.24 ^{+0.14} _{-0.07} 649/455	
0.50- 2.00	EPN	14T			8.0 ^{+0.4} _{-0.5}	0.46 ^{+0.11} _{-0.10}	0.17	1.68 ^{+0.13} _{-0.13}	2.14 ^{+0.12} _{-0.09} 634/445	
2.00- 4.00	EMOS	1T	2.94 ^{+0.06} _{-0.06}		9.5 ^{+0.6} _{-0.5}	0.78 ^{+0.20} _{-0.19}	0.33	1.42 ^{+0.16} _{-0.15}	1.72 ^{+0.10} _{-0.09} 342/294	
2.00- 4.00	EMOS	2T	5.30 ^{+4.35} _{-2.14}	2.42 ^{+0.31} _{-0.89}	9.4 ^{+0.6} _{-0.5}	0.72 ^{+0.19} _{-0.18}	0.39	1.39 ^{+0.16} _{-0.15}	1.63 ^{+0.13} _{-0.11} 324/291	
2.00- 4.00	EMOS	14T			9.3 ^{+0.9} _{-0.4}	0.78 ^{+0.20} _{-0.20}	0.44	1.45 ^{+0.15} _{-0.18}	1.67 ^{+0.09} _{-0.12} 319/281	
2.00- 4.00	EPN	1T	2.84 ^{+0.05} _{-0.05}		7.7 ^{+0.7} _{-0.7}	0.26 ^{+0.17} _{-0.16}	0.22	1.15 ^{+0.17} _{-0.15}	1.56 ^{+0.09} _{-0.08} 491/463	
2.00- 4.00	EPN	2T	37(> 5.0)	2.74 ^{+0.08} _{-0.07}	7.8 ^{+0.6} _{-0.8}	0.25 ^{+0.16} _{-0.15}	0.18	1.13 ^{+0.19} _{-0.13}	1.54 ^{+0.11} _{-0.07} 472/460	
2.00- 4.00	EPN	14T			8.3 ^{+1.7} _{-0.9}	0.34 ^{+0.17} _{-0.19}	0.19	1.11 ^{+0.18} _{-0.14}	1.48 ^{+0.10} _{-0.08} 479/450	
4.00- 8.00	EMOS	1T	3.54 ^{+0.11} _{-0.09}		8.9 ^{+0.6} _{-0.5}	0.43 ^{+0.20} _{-0.19}	0.34	0.78 ^{+0.15} _{-0.14}	0.83 ^{+0.07} _{-0.06} 391/332	
4.00- 8.00	EMOS	2T	6.32 ^{+7.99} _{-4.15}	2.76 ^{+0.55} _{-0.58}	8.8 ^{+0.6} _{-0.6}	0.41 ^{+0.19} _{-0.18}	0.32	0.76 ^{+0.15} _{-0.14}	0.80 ^{+0.10} _{-0.09} 377/329	
4.00- 8.00	EMOS	14T			9.1 ^{+1.0} _{-0.7}	0.41 ^{+0.18} _{-0.18}	0.35	0.78 ^{+0.16} _{-0.14}	0.80 ^{+0.09} _{-0.07} 377/319	
4.00- 8.00	EPN	1T	3.56 ^{+0.10} _{-0.10}		6.4 ^{+0.8} _{-0.6}	0.03 ^{+0.20} _{-0.03}	0.33	0.58 ^{+0.18} _{-0.17}	0.82 ^{+0.07} _{-0.06} 541/534	
4.00- 8.00	EPN	2T	3.57 ^{+0.12} _{-0.09}	0.84 ^{+0.53} _{-0.36}	6.9 ^{+0.8} _{-0.9}	0.12 ^{+0.27} _{-0.12}	0.36	0.60 ^{+0.21} _{-0.16}	0.83 ^{+0.11} _{-0.06} 536/531	
4.00- 8.00	EPN	14T			6.9 ^{+1.5} _{-0.9}	0.15 ^{+0.22} _{-0.15}	0.38	0.62 ^{+0.17} _{-0.17}	0.82 ^{+0.07} _{-0.07} 535/521	
2.00- 8.00	EMOS	1T	3.26 ^{+0.06} _{-0.05}		9.3 ^{+0.3} _{-0.3}	0.55 ^{+0.12} _{-0.12}	0.33	0.99 ^{+0.09} _{-0.09}	1.14 ^{+0.05} _{-0.05} 539/387	
2.00- 8.00	EMOS	2T	6.17 ^{+2.56} _{-1.11}	2.60 ^{+0.28} _{-0.24}	9.2 ^{+0.3} _{-0.3}	0.52 ^{+0.11} _{-0.11}	0.32	0.97 ^{+0.08} _{-0.08}	1.10 ^{+0.07} _{-0.06} 495/384	
2.00- 8.00	EMOS	14T			9.2 ^{+0.6} _{-0.3}	0.52 ^{+0.13} _{-0.11}	0.34	0.98 ^{+0.08} _{-0.09}	1.08 ^{+0.05} _{-0.05} 502/374	
2.00- 8.00	EPN	1T	3.23 ^{+0.08} _{-0.02}		7.1 ^{+0.3} _{-0.7}	0.13 ^{+0.13} _{-0.13}	0.28	0.83 ^{+0.17} _{-0.10}	1.15 ^{+0.06} _{-0.03} 825/686	
2.00- 8.00	EPN	2T	3.18 ^{+0.05} _{-0.04}	0.86 ^{+0.37} _{-0.22}	7.6 ^{+0.4} _{-0.7}	0.19 ^{+0.17} _{-0.10}	0.27	0.82 ^{+0.15} _{-0.08}	1.12 ^{+0.07} _{-0.03} 809/684	
2.00- 8.00	EPN	14T			7.7 ^{+0.7} _{-1.0}	0.22 ^{+0.13} _{-0.14}	0.26	0.80 ^{+0.06} _{-0.09}	1.05 ^{+0.07} _{-0.04} 801/674	

4. Uncertainties in the abundance determination

In the abundance determination, we must examine uncertainties such as the dependence on the plasma code and on the background subtraction. In this section, we study these uncertainties and also calibrate the abundances with the strengths of the lines.

4.1. The effect of the plasma code

In order to constrain the effect of the plasma code on the abundance determination, we compared the results from the APEC (Smith et al. 2001) model with those from the MEKAL model. We used the APEC version 1.1 model in XSPEC version 11.2. As in the MEKAL model fit, we fitted the deprojected spectra with a single, and a multi-temperature APEC model.

The results are summarized in Table 3. With the APEC model, the fit to the Fe-L/Mg-K region at 1.2–1.5

keV improved from that with the MEKAL code (Figure 1). As a result, the reduced χ^2 are consistent or slightly smaller than those from the MEKAL model fit. The derived temperatures, hydrogen column densities, and the Si and Fe abundances are consistent within 10% with those from the MEKAL code (Figure 5, 6).

However, the O and the Mg abundances increased by $\sim 20\%$ and $\sim 80\%$, respectively, from the MEKAL model fit. The difference in the O abundance is consistent with the difference of the strength of the H-like O line between the APEC and MEKAL models, since at 2 keV, that of APEC is 10% larger than that of MEKAL model, and at 4 keV, the difference increases to 30%. The difference in the Mg abundance is not due to the difference in the strength of the Mg-K line between the two codes which is smaller than that of O below 4 keV. It should be caused by the difference in the Fe-L modeling around the Mg-K line. We will discuss it later in §4.3.2.

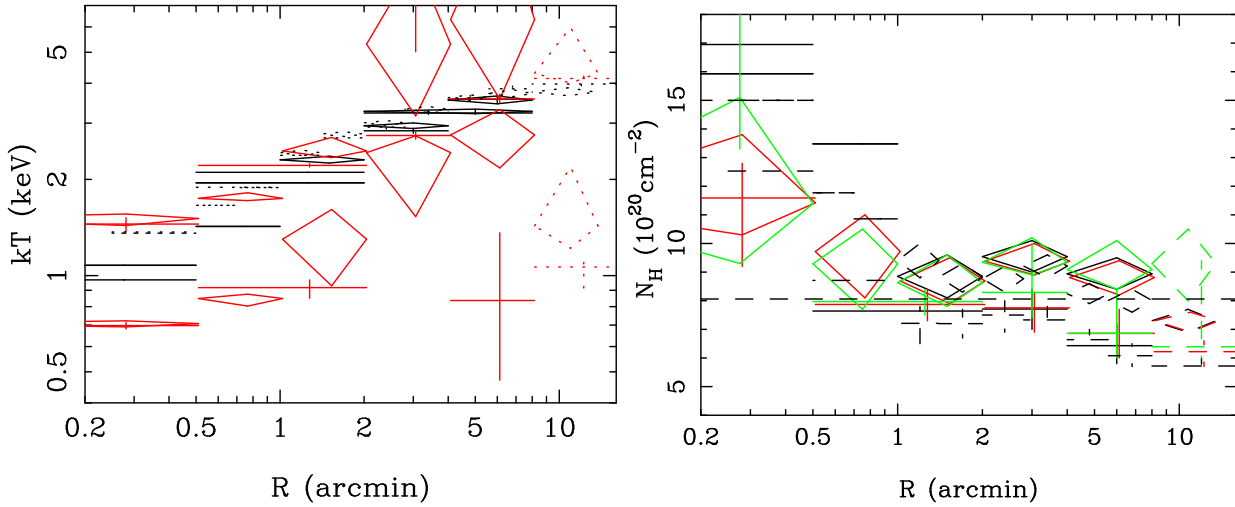


Fig. 2. The radial profiles of the temperature and the hydrogen column density. Dotted and solid lines correspond to the results of the projected spectra and the deprojected spectra, respectively. Black, red and green correspond to the single, two, and the multi-temperature MEKAL model, respectively. The results from the EMOS are shown in diamonds and those from the EPN are shown in crosses. The dashed horizontal line in the profile of the hydrogen column density represents the Galactic value.

Table 3. Results of spectrum fitting of the deprojected spectra within $8'$ and projected spectrum at $8\text{--}13.5'$ of the EMOS with the single- and the multi-temperature APEC model.

R (arcmin)		kT (keV)	N_{H} (10^{20}cm^{-2})	O (solar)	Mg (solar)	Si (solar)	Fe (solar)	χ^2/dof
0.00- 0.50	EMOS	1T	1.00	17.1	0.36	0.23	0.27	676/129
0.00- 0.50	EMOS	14T		$10.6^{+2.7}_{-1.5}$	$0.50^{+0.23}_{-0.21}$	$1.45^{+0.49}_{-0.49}$	$1.47^{+0.34}_{-0.40}$	$1.72^{+0.19}_{-0.36}$ 146/116
0.50- 2.00	EMOS	1T	1.93	11.1	0.47	0.68	1.35	585/249
0.50- 2.00	EMOS	14T		$9.3^{+0.6}_{-0.7}$	$0.91^{+0.21}_{-0.19}$	$1.54^{+0.15}_{-0.24}$	$2.29^{+0.25}_{-0.20}$	$2.42^{+0.20}_{-0.16}$ 266/236
2.00- 4.00	EMOS	1T	$2.94^{+0.06}_{-0.06}$	$9.8^{+0.6}_{-0.5}$	$0.96^{+0.27}_{-0.25}$	$0.89^{+0.28}_{-0.27}$	$1.46^{+0.17}_{-0.16}$	$1.83^{+0.11}_{-0.10}$ 346/294
2.00- 4.00	EMOS	14T		$9.5^{+0.7}_{-0.6}$	$1.00^{+0.26}_{-0.25}$	$0.89^{+0.28}_{-0.25}$	$1.49^{+0.19}_{-0.16}$	$1.76^{+0.13}_{-0.12}$ 301/281
4.00- 8.00	EMOS	1T	$3.53^{+0.11}_{-0.11}$	$9.1^{+0.6}_{-0.5}$	$0.61^{+0.27}_{-0.26}$	$0.62^{+0.31}_{-0.30}$	$0.84^{+0.16}_{-0.16}$	$0.92^{+0.08}_{-0.08}$ 397/332
4.00- 8.00	EMOS	14T		$9.1^{+0.5}_{-0.7}$	$0.54^{+0.27}_{-0.23}$	$0.58^{+0.32}_{-0.28}$	$0.84^{+0.18}_{-0.15}$	$0.88^{+0.10}_{-0.08}$ 372/319
8.00-13.50	EMOS	1T	$3.77^{+0.10}_{-0.10}$	$7.4^{+0.4}_{-0.4}$	$0.52^{+0.18}_{-0.18}$		$0.67^{+0.12}_{-0.11}$	$0.63^{+0.06}_{-0.06}$ 443/325
8.00-13.50	EMOS	14T		$8.7^{+1.1}_{-1.1}$	$0.38^{+0.18}_{-0.16}$		$0.72^{+0.13}_{-0.12}$	$0.60^{+0.08}_{-0.07}$ 388/312

4.2. Effect of the background uncertainty

One of the most severe problems in analyzing XMM-Newton data are uncertainties in the background. In this paper, we adopted deep survey data as a background, which agree well with the data of the Centaurus cluster above 8 keV (Figure 7). In addition, in order to study the effect of the uncertainty of the background, we artificially scaled the background by 10%, and fitted the projected EMOS spectra at $r > 2'$ in the same way as previously. Since spectral variations of the background amount to about 10% below 1 keV when the background is scaled with the count-rate outside the field of the view of the detector (Katayama et al. 2004), and the relatively high Galactic N_{H} towards the Centaurus cluster absorbs the low energy photons from the Cosmic X-ray Background (CXB).

The results are summarized in Figure 8. Within $8'$, the derived temperatures, the Fe abundances, the O/Fe and the Si/Fe ratios are consistent within a few % with

those derived from the background used in §3.1. Outside $8'$, the 10% change of the background changes derived parameters by $\sim 10\%$. Therefore, the background problem is not severe in this observation.

4.3. Comparisons between the line strength and model fit

4.3.1. The line strengths of O and Si and the abundance determination

In order to study the discrepancy in the O and the Si abundances between the EMOS and the EPN data, it is important to check their line strengths directly. Complications arise since the energy resolution of the EMOS has become worse due to the radiation damage in orbit (Kirsh 2002), and that of the EPN depends on the distance from the read-out. In addition, there are still discrepancies of several % in the response matrix between the EPN and

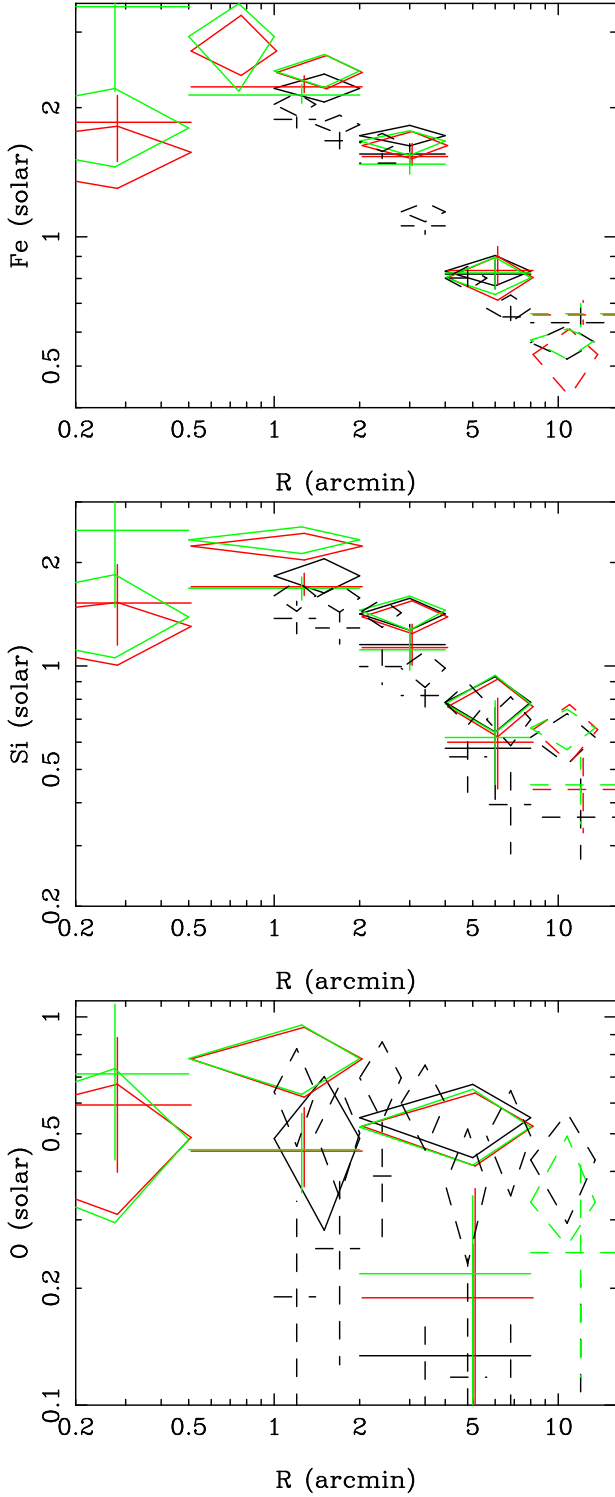


Fig. 3. Radial profiles of the abundances of Fe, Si and O. The meanings of symbols are the same as those of Figure 2. The data with a reduced $\chi^2 > 2$ are not shown.

EMOS, which might give a large uncertainty in strengths of weak lines.

The strengths of K α lines of H-like O and Si are derived from fittings of the spectra around the lines with Gaussians. The details are the same as in Matsushita et al. (2003). First, the line widths of the Gaussians were

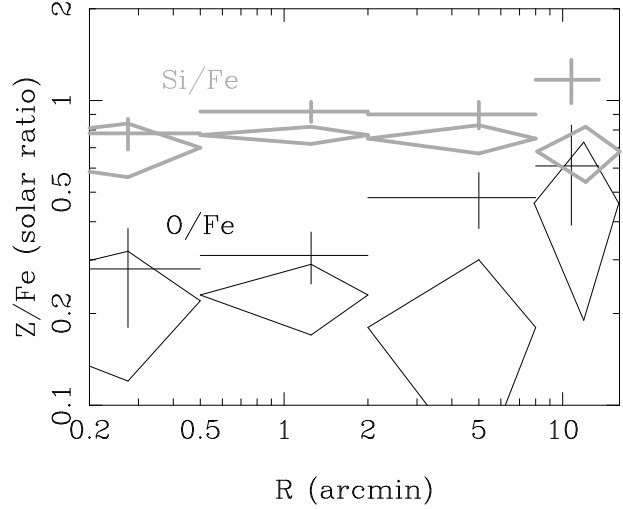


Fig. 4. Radial profiles of the O/Fe (black lines) and the Si/Fe (gray lines) ratios in units of the solar elemental ratio derived from the multi-temperature MEKAL model of the EMOS (diamonds) and the EPN (crosses) spectra.

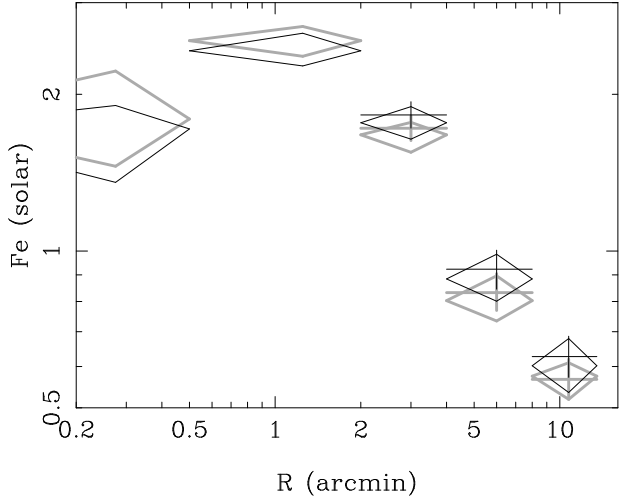


Fig. 5. The Fe abundance profile derived from the MEKAL (gray data) and the APEC (black data) model, from the single-temperature model (crosses) and the multi-temperature model (diamonds). The data with a reduced $\chi^2 > 2$ are not shown.

frozen to zero, and then allowed to be free. Figure 9 compares the best fit MEKAL model and the Gaussian fits for representative spectra at $R=2-8'$. In the EMOS spectrum, we can see a weak bump of the H-like O line, and a clear bump of the H-like Si line. In contrast, in the spectrum of the EPN, which has an energy resolution worse than that of the EMOS, the continuum and the O line are hardly distinguished and the Si line is much broader than the EMOS one.

For the EMOS spectra, the line strengths of K α of H-like O and Si from the Gaussian fits are consistent within 10% with the those from the MEKAL model, except for the O line strength within 0.5', where the O line is com-

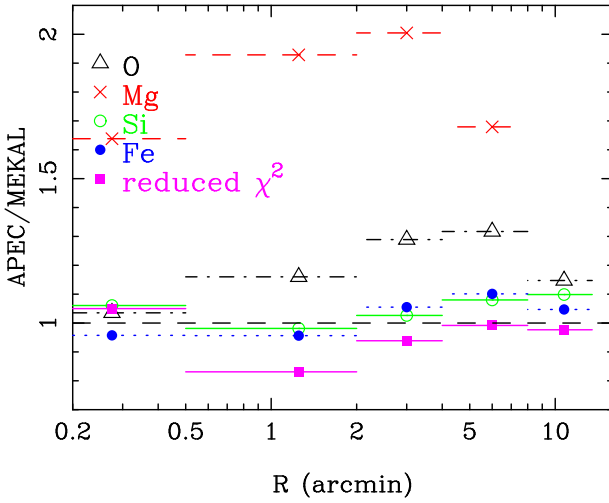


Fig. 6. The ratio of the O(open triangles), Mg(crosses), Si(open circles) and Fe(closed circles) abundances and the reduced χ^2 (closed boxes) between the multi-temperature APEC and the multi-temperature MEKAL model.

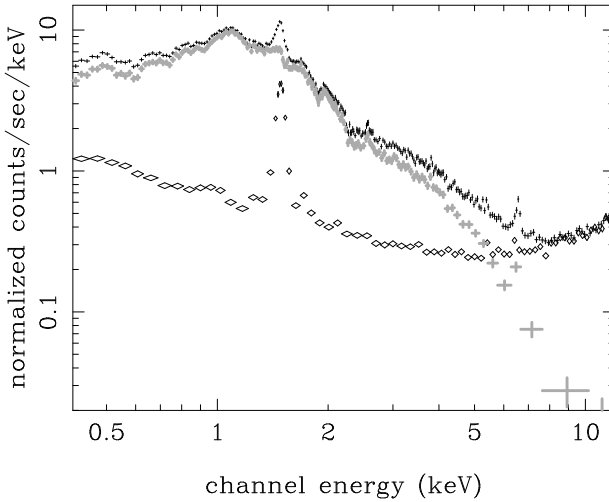


Fig. 7. The raw EMOS spectrum at $r > 8'$ (black crosses) and the adopted background spectrum (black diamonds), and the background subtracted spectrum (gray crosses).

pletely hidden in the Fe-L lines (Figure 10). This result indicates that the effect of the decrease of the energy resolution of the EMOS detector should not affect the derived O and Si abundances.

In contrast, allowing the line width to be a free parameter, the Gaussian fits to the EPN spectra give systematically larger line strengths than the MEKAL model fit. As a result, adopting the values from the Gaussian fits, the EPN abundances become consistent with the EMOS ones. Therefore, the O and Si abundances derived from the EMOS fit should be reliable, since it has a better spectral resolution and it gives consistent strengths of the $K\alpha$ lines between the Gaussian fits and the MEKAL model fits.

As shown in the Figure 11, the ratio of strengths of $K\alpha$ lines of H-like O and Si becomes constant above 1.7 keV and increases toward lower energies. This temper-

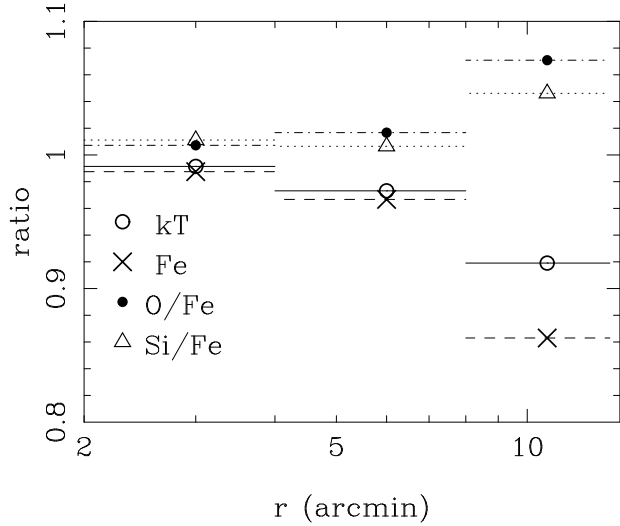


Fig. 8. The ratio of derived parameters of the projected EMOS spectra with the multi-temperature model using a background scaled by a factor of 1.1 to those using the unscaled background used in the paper.

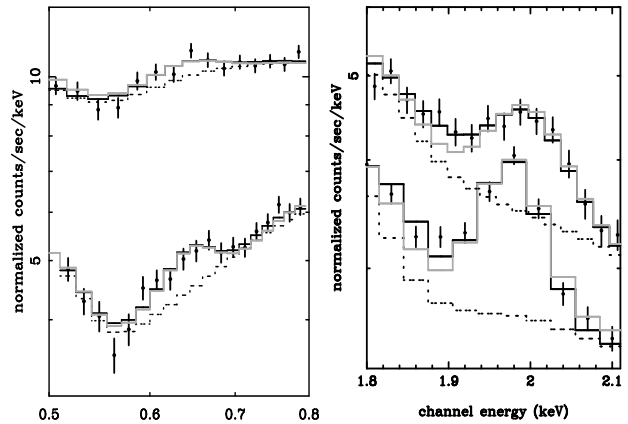


Fig. 9. Deprojected spectra of the EMOS (EMOS1+EMOS2; lower curve) and the EPN (upper curve) at $R=2.0-8.0'$ around the energy of the lines of O (left panel) and Si (right panel). The gray data points and black solid lines correspond to the best fit model with one temperature MEKAL model and that with Gaussians with 0 line widths, respectively. The black dotted lines represent the continuum emissions as described by the Gaussian fit.

ature dependence means that any temperature distribution cannot yield a O/Si ratio larger than 0.6 solar within 4'. Furthermore, we got a higher value of the line ratio at $R > 8'$ by a factor of 2. It implies that the O/Si ratio increases in the region, since the contribution to the O line from the component below 1.7 keV of the multi-temperature MEKAL model is smaller than 10%.

4.3.2. The line strength of the Mg-K

It is also important to derive the strengths of the $K\alpha$ -lines of Mg directly, since the Mg abundances derived from the

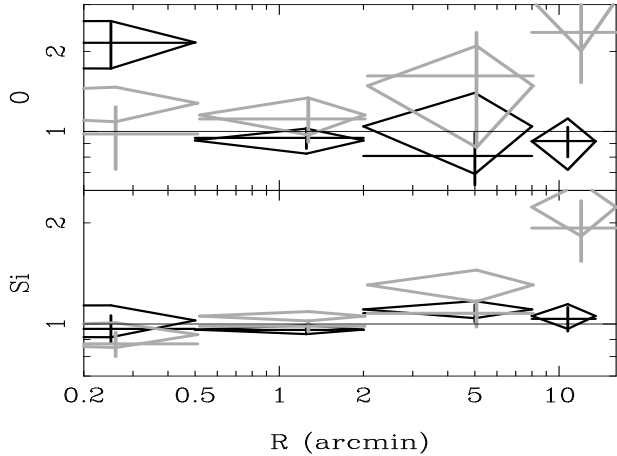


Fig. 10. The ratio of line strengths $K\alpha$ of H-like O (upper panel) and Si (lower panel) derived from the Gaussian fit to those of best fit values from spectral fit for the EMOS (black lines) and EPN (gray lines). Crosses and diamonds correspond to the fitting with a Gaussian with 0 line width and free line width, respectively. Errors correspond the 68% level.

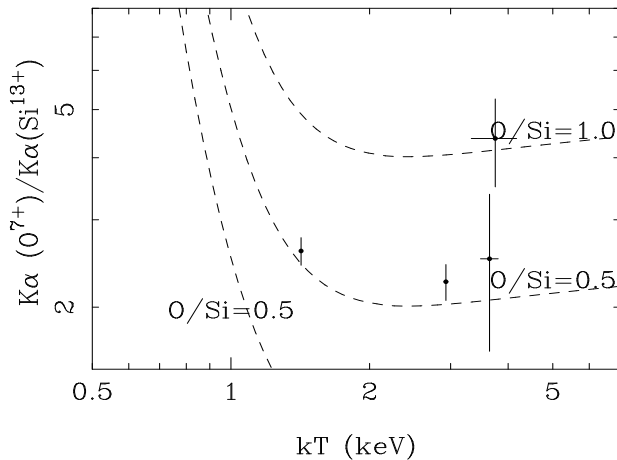


Fig. 11. The line ratios of $K\alpha$ lines of H-like O and Si of the projected spectra of the EMOS, plotted against the best fit temperature fitted with the single MEKAL model. Dashed lines correspond to constant abundance ratios in units of the solar ratio. Errors represent the 68% confidence level.

spectral fits depend on the modeling of the underlying Fe-L lines. We therefore fitted the EMOS spectra within the energy range of 1.3–1.65 keV with Gaussians plus one- or two- or three-temperature MEKAL or APEC model.

All of the Gaussian models can fit the spectra around the Mg-K/Fe-L region well (Figure 12). The derived strengths of the $K\alpha$ -line of H-like and He-like Mg do not depend on the temperature structure (i.e. one-, two, or three-temperature model) or the plasma code (i.e. MEKAL or APEC model). The line strengths agree well with those derived from the fitting the spectra described in §4.1, but are systematically higher than those derived from the multi-temperature MEKAL model described in §3,

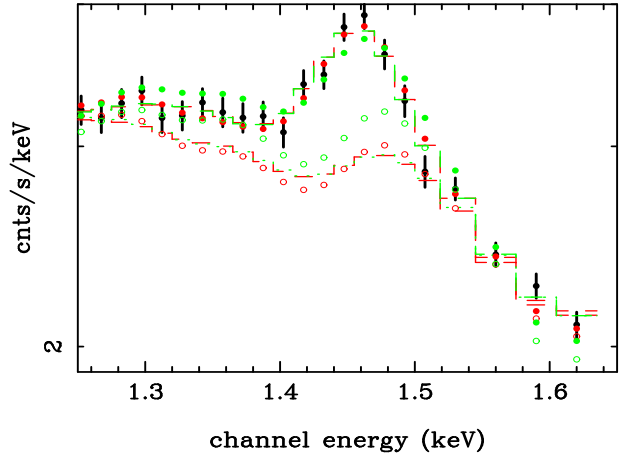


Fig. 12. The deprojected spectrum of the EMOS at $R=0.5-2.0'$ (black closed circles) fitted with the multi-temperature MEKAL model (green closed circles), the multi-temperature APEC model (red closed circles), the Gaussians with MEKAL models (green dashed lines) and the Gaussians with the APEC models (red dashed lines). The contributions of the continuum plus the Fe-L are also shown for the multi-temperature APEC model (red open circles) and the multi-temperature MEKAL model (green open circles) and the Gaussian fit (red and green dashed lines).

which cannot reproduce the spectra around the Mg-K/Fe-L region (Figure 13). Therefore, it is reasonable to adopt the Mg abundances derived from the multi-temperature APEC model fit as the Mg abundances of the ICM.

We note that the Mg/O ratio does not depend on the temperature structure since the line ratio of $K\alpha$ lines of these two elements is nearly constant above 1.1 keV (Matsushita et al. 2003).

4.3.3. The line strength of Fe-K

Since the temperature dependence of the intensities of the Fe-L and Fe-K lines is completely different, a comparison between the Fe-L and the Fe-K lines strongly constrains the temperature structure and the Fe abundance. In the spectral fitting by the MEKAL model or the APEC model, the strengths of the 6.7 keV Fe-K lines are fitted well, although the fit to the Fe-L lines mostly determines the Fe abundance due to its high statistics (Figure 14).

When the Fe abundance is shifted by 40% in the fits with the multi-temperature model, the Fe-L structure can be roughly fitted although the χ^2 increased significantly (Figure 14). However, the strengths of the Fe-K line cannot be reproduced. Therefore, the uncertainties in the Fe-L line fit, due to the temperature structure and the plasma code should not be severe problems at least in the Centaurus cluster.

Since abundances derived from the Fe-K line may have an uncertainty due to the uncertainty of the background, we have also derived the line strength of the Fe-K line di-

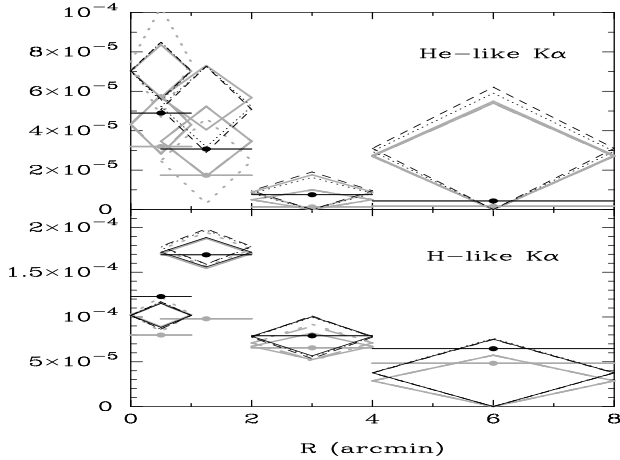


Fig. 13. The profile of the line strengths of the K α -line of He-like and H-like Mg of the best fit model of the multi-temperature model (horizontal solid lines) and derived from the Gaussians plus a single temperature model (solid diamonds), two temperature model (dashed diamonds), and three-temperature model (dotted diamonds). The gray and black data correspond to the MEKAL and APEC model, respectively. Errors correspond to the 68% confidence level.

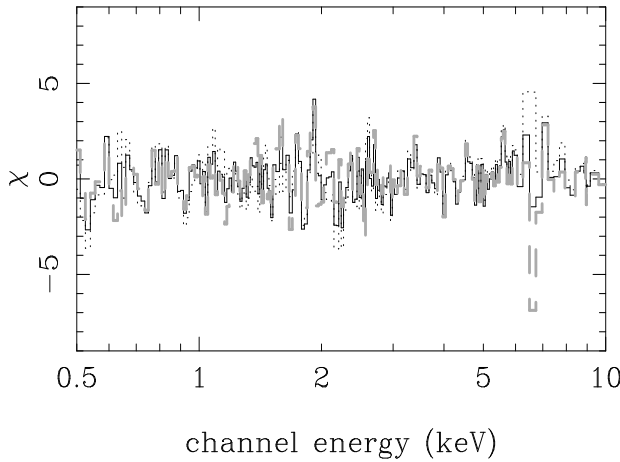


Fig. 14. The χ distributions of the deprojected spectrum at $R=0.5-2.0'$ fitted with the multi-temperature APEC model. The solid black line corresponds to the best fit model, and the dotted black line and dashed gray lines correspond to the model where the Fe abundance is fixed to be 1.6 solar and 3.2 solar, respectively.

rectly from a Gaussian fit. The width of the Gaussian was allowed to be a free parameter, since the 6.7 keV Fe-K consists of several strong lines. In figure 15, the derived line strengths from the Gaussian fit are compared to the line strengths of the Fe-K line derived from the best fit multi-temperature MEKAL model. These values agree within 10%. Thus, the line strengths of the Fe-K line are consistent with the Fe abundances derived from the MEKAL model fit and a change of the Fe abundance cannot reproduce the observed line strength of the Fe-K.

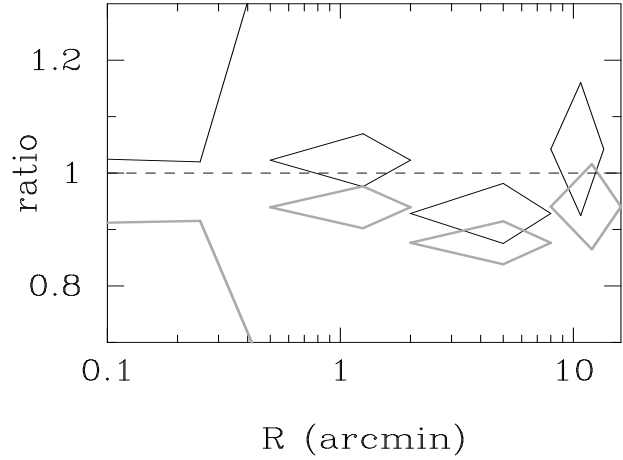


Fig. 15. The ratio of line strengths of the 6.7 keV Fe-K line derived from the Gaussian fit to those of best fit values from spectral fit for the EMOS (black lines) and EPN (gray lines), where the Fe-L is important to determine the Fe abundance. Errors correspond to the 68% level.

5. Discussion

5.1. Summary of the results

The abundances of O, Mg, Si, and Fe in the ICM of the Centaurus cluster are derived. We have checked uncertainties in the temperature structure, in the background subtraction, and in the spectral model and studied their effects on the abundance determination. The Fe abundance is ~ 2.3 solar within $2'$ and decreases to ~ 0.6 solar at $R > 8'$. The Si abundance is close to the Fe abundance. In contrast, the O and Mg abundances are much smaller than the Fe and Si abundances in units of the solar ratio.

The abundance pattern of the ICM of the Centaurus cluster, the low O abundance compared to those of Si and Fe, resembles to those observed in center of other clusters and groups of galaxies, such as M 87 (Matsushita et al. 2003), A496 (Tamura et al. 2001b), Fornax cluster (Buote et al. 2002) and group-center elliptical galaxies NGC 4636 (Xu et al. 2002), NGC 5044 (Tamura et al. 2003; Boute et al. 2003). However, there are small differences in the observed abundance pattern of the ICM. For example, the central Fe abundance of the Centaurus cluster (2.3 solar) is 40% larger than that of M 87 (1.6 solar). In addition, the Si/Fe ratio of the former is 20% smaller than that of the latter. In this section, we mainly compare and discuss the abundance pattern of the Centaurus clusters with that of M 87, since these two clusters are the nearest and the best studied objects among relatively low temperature clusters.

5.2. Comparison with stellar metallicity and SN II abundance pattern

The O and Mg in the gas around a cD galaxy is a mixture of those in the ICM and those in the accumulation of stellar mass loss from the cD galaxy, since these elements are only synthesized by SN II. The O and Mg abundances

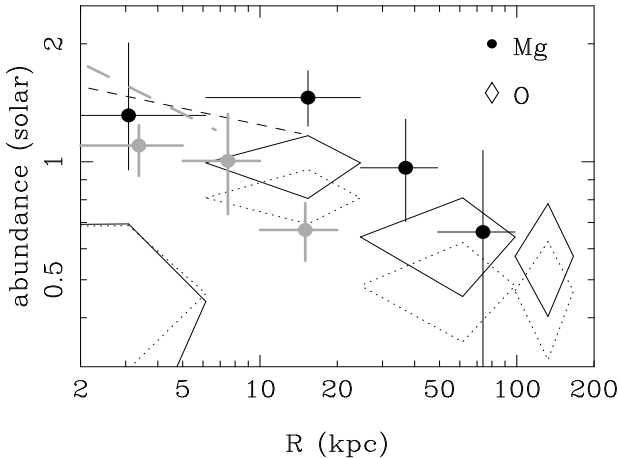


Fig. 16. Mg (closed circles) and O (diamonds) abundances derived for the Centaurus cluster (black) and M 87 (gray) from the multi-temperature MEKAL (dotted lines) and APEC (solid lines) model. The dashed lines represent the stellar metallicity of NGC 4696 (black) and M 87 (gray) derived from the optical Mg₂ index (Kobayashi & Arimoto 1999).

of the mass loss reflect those of mass losing stars, which contribute significantly to the optical light from elliptical galaxies. The stellar metallicity of elliptical galaxies are usually derived from the Mg₂ index in the optical spectra, which depends mainly on the Mg abundance and stellar metallicity where O contributes most, and weakly on the age population of stars. Therefore, comparing the O and Mg abundances of the gas and stellar metallicity derived from the optical Mg₂ index is important to study the gas flow and contribution of stellar mass loss, and stellar metallicity of the cD galaxies.

The Mg abundances of the two clusters are close to their stellar metallicity derived from the Mg₂ index (Figure 16; Kobayashi & Arimoto 1999). The gradient of the Mg abundance of the gas around M 87 is steeper than in the Centaurus cluster. At a radius of 10–20 kpc, the Mg abundance of the Centaurus cluster is a factor of 2 larger than that of M 87 (Figure 16). The stellar metallicity gradient of M 87 is also steeper than that of NGC 4696, the cD galaxy of the Centaurus cluster. The agreements of between the Mg abundances with stellar metallicity at the central regions indicates that in these regions, the gas is dominated by gas ejected from the cD galaxies.

The Mg/O ratio of the gas of the Centaurus cluster is 1.2 ± 0.3 of the solar ratio on average as determined with the multi-temperature APEC model. This value is close to that of the ICM within 4' of M 87, which is 1.3 ± 0.1 solar ratio (Matsushita et al. 2003), and also to the value of 1.3 ± 0.2 solar ratio of NGC 4636 (Xu et al. 2003) derived from the RGS. The observed Mg/O ratios of the gas at the cluster centers are close to [Mg/O] of the Galactic stars (Edvardsson et al. 1993). Therefore, at least for the Mg/O ratio, the Galactic SN II and those trapped in stars in the cD galaxies have no difference.

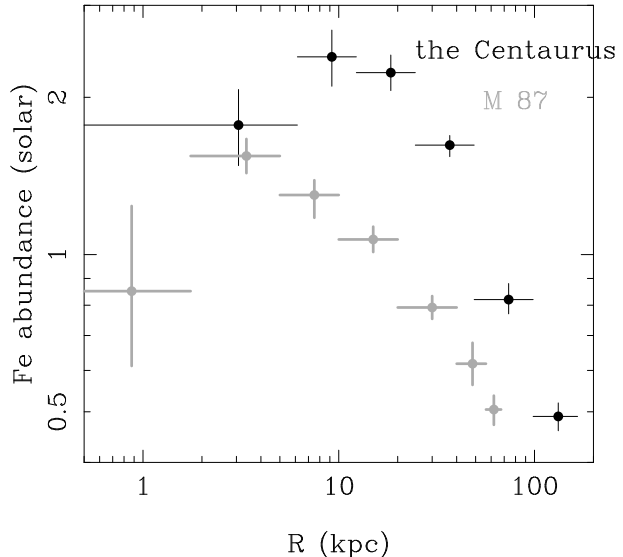


Fig. 17. The Fe abundance of the ICM of the center of Centaurus cluster (black) and M 87 (gray).

5.3. The Fe abundance profile and SN Ia contribution

The Fe in the gas at the core of clusters is also a mixture of those in the ICM and the recent supply from the cD galaxy. The latter contains Fe synthesized by SN Ia and those coming from stars through stellar mass loss, since Fe is synthesized by both SN Ia and SN II.

The Fe abundance of the ICM of the Centaurus cluster is systematically higher than that around M 87 at a same distance from the cluster center (Figure 17). The peak Fe abundance of the Centaurus cluster is 2.3 solar. This value is significantly higher than that of M 87, which is 1.6 solar. Assuming that the O/Fe ratio of SN II is 3, the central Fe abundances from SN Ia of the Centaurus cluster and M 87 become 2 and 1.3 solar, respectively. Since the SN Ia contribution to the Fe abundance is dominant, the uncertainty in the assumption for the O/Fe ratio does not change the result very much.

The Fe abundance of gas from SN Ia in an elliptical galaxy is proportional to $M_{\text{SN}}^{\text{Fe}} \theta_{\text{SN}} / \alpha_*$ (see Matsushita et al. 2003 for details). Here, $M_{\text{SN}}^{\text{Fe}}$ is the mass of Fe synthesized by one SN Ia, θ_{SN} is SN Ia rate, and α_* is stellar mass loss rate. The higher Fe abundance of the gas in the central region of the Centaurus cluster indicates a higher $M_{\text{SN}}^{\text{Fe}} \theta_{\text{SN}} / \alpha_*$. The cooling flow rate derived from the standard cooling flow model is higher in the Centaurus cluster (Allen & Fabian 1994) than that of the M 87 (Matsushita et al. 2002). Böhringer et al. (2004) questioned the standard cooling flow model comparing the Fe mass profile of 4 clusters of galaxies with cooling cores including M 87 and the Centaurus cluster. They concluded that we need long enrichment times (> 5 Gyr) in order to accumulate the observed Fe abundance peak even if the SN Ia rate was larger in the past.

As shown in Figure 18, a difference between M 87 and the Centaurus cluster is the ratio of the Fe mass to the

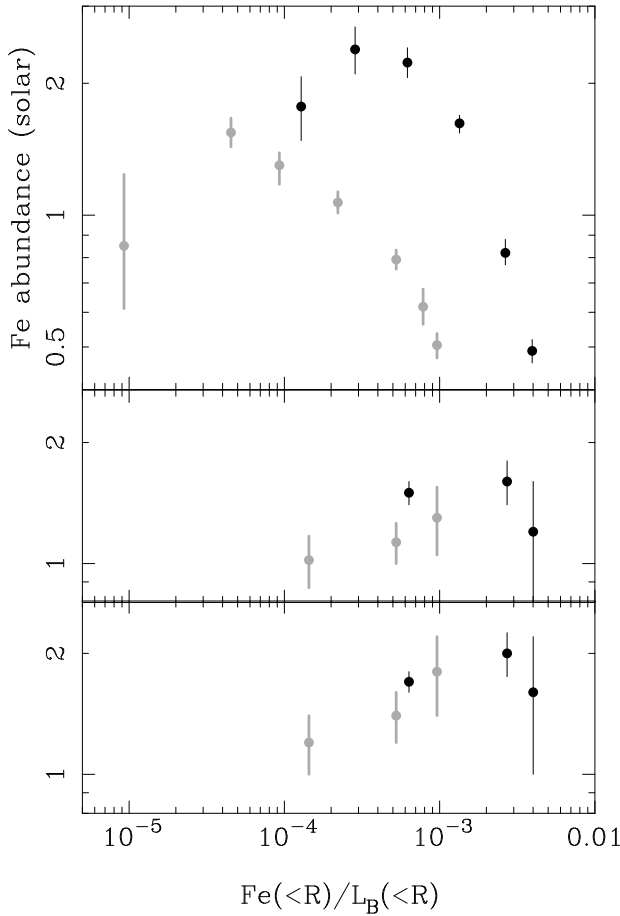


Fig. 18. The Fe abundance (the upper panel) and $(Fe/Si)_{SNIa}$ (the middle and the bottom panel) in units of the solar values are plotted against the ratio of the Fe mass to B-band luminosity of the cD galaxy (IMLR), for M 87 (gray circles) and the Centaurus cluster (black circles), when adopting the abundance pattern of SN II from the average value of Galactic metal poor stars (the middle panel; Clementini et al. 1999) and from nucleosynthesis model (the bottom panel) by Nomoto et al. (1997) assuming Salpeter's initial mass function (Iwamoto et al. 1999).

stellar B-band luminosity of the cD galaxy (IMLR). The total B-band luminosity and the effective radius were calculated using Prugniel and Heraudeau (1998), and the effect of the Galactic extinction was corrected using Schlegel et al. (1998). The IMLR of the Centaurus cluster is much higher than that of the M 87, especially within the central region. Since the contribution of the SN Ia to Fe in the ICM is dominant, this indicates that accumulation time scale of SN Ia is higher in the Centaurus cluster than that in M 87, although we do not know the actual gas flow rate due to the cooling flow problem. The longer accumulation time scale in the Centaurus cluster means that $M_{SN}^{Fe} \theta_{SN} / \alpha_*$ was higher in the past. In other words, the Fe mass synthesized by a SN Ia was higher in the past or the ratio of SN Ia rate to stellar mass loss rate was higher in the past as suggested in Renzini et al. (1993).

5.4. Abundance pattern of SN Ia

Si is both synthesized by SN Ia and SN II, and the abundance pattern of O, Si, and Fe strongly constrains the nucleosynthesis of the SN Ia when Fe is dominated by SN Ia. Figure 19 summarizes the ratio of these three elements in the ICM of the Centaurus cluster and M 87 (Matsushita et al. 2003). As in M 87, the data of the Centaurus cluster cannot be explained by a sum of SN II abundance pattern in the Galactic metal poor stars (Clementini et al. 1999), and SN Ia abundance pattern by the W7 model. The Si abundances are clearly higher than the sum of the two.

At the cluster center, the Fe/Si ratio and the Fe/O ratio of the gas of the Centaurus cluster are systematically higher than those of M 87, respectively. The main difference between M 87 and the Centaurus Cluster is the IMLR as described in the previous section. In figure 18, $(Fe/Si)_{SNIa}$ is also plotted against IMLR. The derived $(Fe/Si)_{SNIa}$ value is much smaller than the value of 2.6 in units of the solar ratio which is predicted by the W7 model. Regions with larger IMLR have larger values of $(Fe/Si)_{SNIa}$, when adopting the SN II pattern of either the Galactic stars (Clementini et al. 1999), or the nucleosynthesis model (Iwamoto et al. 1999). A larger IMLR corresponds to a longer accumulation time scale. For M 87, it needs only a few Gyr to accumulate the observed gas mass within 10 kpc where the gas from the cD galaxy is dominant (Matsushita et al. 2002). In contrast, in the center of the Centaurus cluster, ejecta of SN Ia are accumulated over a much longer time scale than that of M 87. Therefore, the correlation between $(Fe/Si)_{SNIa}$ and IMLR support the suggestion by Finoguenov et al. (2002) and Matsushita et al. (2003) from the M 87 observation that $(Fe/Si)_{SNIa}$ depends on the age of the system. Matsushita et al. (2003) discovered that the Si/O ratio of the Galaxy also increases systematically toward metal rich stars. This result indicates that there is a source of high Si/O ratio in our Galaxy at present and supports the scenario suggesting a dependency of the Fe/Si ratio of ejecta of SN Ia on the age of the system.

5.5. The hydrogen column density and the cooling flow model

In the ASCA era, in order to explain observed fluxes of soft energy photons which are much smaller than the expected value from the standard cooling flow model, absorption within cluster cores was discussed (Allen et al. 2001). In order to obscure a cooling flow in the Centaurus cluster from the standard model, we need at least additional column density around $2 \times 10^{21} \text{ cm}^{-2}$. However, with the XMM-Newton observations, the observed hydrogen column density is too low to conceal the cool component from the cooling flow model (Matsushita et al. 2002, Böhringer et al. 2002). The observed hydrogen column density of the Centaurus cluster is also consistent with the Galactic value, $8.06 \times 10^{20} \text{ cm}^{-2}$ over the whole field

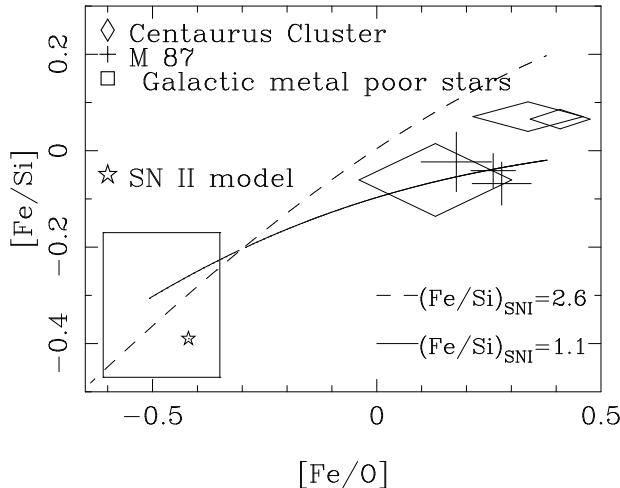


Fig. 19. [Fe/Si] of the ICM of the Centaurus cluster (diamonds) and M 87 (crosses; Matsushita et al. 2003) are plotted against [Fe/O]. The average value of Galactic metal poor stars (Clementini et al. 1999; open square) and the abundance ratio of SN II model using the nucleosynthesis model (asterisk) derived in Nomoto et al. (1997), assuming Salpeter's IMF (Iwamoto et al. 1999) are shown. The solid line and dashed line represent the relation of the abundance pattern synthesized by SN Ia with Fe/Si=1.1 (the best fit relation of M 87) and Fe/Si=2.6 (W7 ratio; Nomoto et al. 1984), respectively.

of view. This means that the soft energy photons from the Centaurus cluster are not obscured.

6. Conclusion

With the XMM-Newton observation, the abundance pattern of O, Mg, Si, and Fe of the ICM of the Centaurus cluster are derived. At the very center, the Mg and O abundances are close to the stellar metallicity. This result indicates that the gas at the very center is dominated by the supply of the stellar mass loss from the cD galaxy.

The abundances of Si and Fe are close to each other in units of the solar abundance, while the O and Mg abundances are smaller, like in the centers of other clusters and groups of galaxies. In order to explain the abundance pattern, the SN Ia ejecta from the cD galaxy should have a higher Si/Fe ratio than the standard W7 model by Nomoto et al. (1984).

There are small differences in the Fe abundances and the Fe/Si ratio in the ICM between the Centaurus cluster and M 87 (Matsushita et al. 2003). These differences and the higher IMLR in the Centaurus cluster may reflect a higher accumulation time scale of SN Ia. In order to confirm this suspicion, we will further study abundance patterns of the ICM of number of clusters and groups of galaxies with Suzaku which has a better energy resolution at the O lines.

Acknowledgements. This work was supported by Humboldt foundation. The paper is based on observations obtained with

XMM-Newton, an ESA science mission with instruments and contributions direct by funded by ESA Member States and the USA (NASA). The XMM-Newton project is supported by the Bundesministerium für Bildung und Forschung, Deutsches Zentrum für Luft und Raumfahrt (BMBF/DLR), the Max-Planck Society and the Haidenhain-Stiftung.

References

Allen, S. W., & Fabian, A.C., 1994, MNRAS, 269, 409
Allen, S. W., Fabian, A. C., Johnstone, R. M., Arnaud, K. A., & Nulsen, P. E. J. 2001, MNRAS, 322, 589
Böhringer, H., Belsole, E., Kennea, J., et al. 2001, A&A, 365, L181
Böhringer, H., Matsushita, K., Churazov, E. et al. 2002, A&A, 382, 804
Böhringer, H., Matsushita, K., Churazov, E. et al. 2004, A&A, 416, L21
Buote D. A., Jeltema, T. E., Canizares, C. R., et al. 2002, ApJ, 577, 183
Buote D. A., Lewis, A. D., Brighenti, F., et al. 2003, ApJ, 595, 151
Clementini, G., Gratton, R.G., Carretta, E. et al., 1999, MNRAS, 302, 22
Edvardsson, E., Andersen, J., Gustafsson B., et al. 1993, 275, 101
Feldman, U., 1992, Physica Scripta 46, 202
Finoguenov A., Matsushita, K., Böhringer, H., et al. 2002, A&A 381, 21
Fukazawa Y., Ohashi, T., Fabian, A.C. et al. 1994, PASJ, 46, 55L
Hamuy, M., Philips, M.M., Suntzeff, N.B., et al. 1996, AJ, 112, 2438
Ikebe Y., Makishima K. Fukazawa Y. et al., 1999, ApJ, 525, 58
Iwamoto, K., Brachwitz, F., Nomoto, K., et al. 1999, ApJS, 125, 439
Ivanov, V., Hamuy, M., & Pinto, P.A., 2000, ApJ, 542, 588
Kaastra J.S. 1992, An X-Ray Spectral Code for Optically Thin Plasmas (Internal SRON-Leiden Report)
Katayama, H., Takahashi, I., Ikebe, Y., Matsushita, K., & Freyberg, M., 2004, A&A, 414, 767
Kirsh, 2002, XMM-cal-report
Kobayashi, C., & Arimoto, N., 1999, ApJ, 527, 573
Liedahl, D.A., Osterheld, A.L., and Goldstein, W.H. 1995, ApJL, 438, 115
Makishima K., Ezawa H., Fukazawa Y. et al. 2001, PASJ, 53, 401
Matsushita, K., Belsole, E., Finoguenov, A., & Böhringer, H., 2002, A&A, 386, 77
Matsushita K., Finoguenov A., Böhringer H., 2003, A&A, 401, 443
Nomoto, K., Thielemann, F.K., & Wheeler, J.C., 1984, ApJ, 279, 23
Nomoto, K., Hashimoto, M., Tsujimoto, T., et al. 1997, Nuclear Physics A, 616, 79
Nugent P., Baron E., Branch D. et al. 1997, ApJ, 485, 812
Prugniel, P. & Heraudeau, P., 1998, A&AS, 128, 299
Renzini, A., Ciotti, L., D'Ercole, A., et al. 1993, ApJ, 419, 52
Sanders J.S., and Fabian A.C., 2002, MNRAS, 331, 273
Schlegel, D. J., Finkbeiner, D. P., & Davis, M. 1998, ApJ, 500, 525

Smith, R.K., Brickhouse, N.S., Liedahl, D.A., & Raymond, J.S.,
2001, ApJ, 556, 91

Takahashi I. 2004, Ph.D. thesis, University of Tokyo

Tamura T., Kaastra J.S., Peterson et al. 2001a, A&A, 365, L87

Tamura T., Bleeker, J.A.M., Kaastra, J.S., et al. 2001b, A&A,
379, 107

Tamura, T., Kaastra, J. S., Makishima, K., & Takahashi, I.
2003, A&A, 399, 497

Umeda H., Nomoto K., & Kobayashi C. 1999, ApJ, 522, L43

Xu, H., Kahn, S. M., Peterson, J. R., et al. 2002, ApJ, 579,
600